Dynamics of pore flow between shark dermal denticles

By W. Wu† AND B. Savino†

1. Motivation and objectives

Shark dermal scales (see Figure 1) exhibit notable distinctions from those found in bony fish. While the streamwise-oriented ridges on their crown resemble the recognized drag-reducing riblets, researchers have not agreed upon the mechanisms of the hydrodynamic advantages of shark skin. Experimental tests with real shark skin rarely show drag reduction (Bechert *et al.* 1985; Oeffner & Lauder 2012). Similarly, recent direct numerical simulations (DNS) of turbulent channel flows over shark denticle replicas reported an increase in drag (Boomsma & Sotiropoulos 2016; Lloyd *et al.* 2023). Meanwhile, there has been a growing interest in exploring the potential of denticles to reduce pressure drag by controlling flow separation during self-propelling maneuvers. A series of works by Lang and co-workers focused on a denticle's ability to bristle (Lang *et al.* 2008, 2011; Du Clos *et al.* 2018; Santos *et al.* 2021). They hypothesized that the bristling is activated by reversed flow and it modulates flow separation by 1) creating extended protrusion of the trailing edge of the denticle crown into the flow and 2) forming cavities and local vortices between denticles. Evans *et al.* (2018) and Doosttalab *et al.* (2018) simplified the shark denticles as diverging pillars and placed an array of them on the lee sides of an expanding channel and an airfoil. They observed a delay in the onset of separation as well as an overall reduction in separation size. It was hypothesized that the forward pore flow between the pillars creates local unsteady suction and blowing. However, these mechanisms were not well justified due to the lack of data in the vicinity of the denticles, especially beneath the crown.

While the specific mechanisms underlying the modulation of separation by shark denticles remain unclear, engineers have actively explored the impact of these structures on aerodynamic performance in various engineering applications. Nevertheless, the outcomes are markedly influenced by factors such as the airfoil configuration, the size of biomimetic denticles, and their positioning in relation to the separation point (Devey *et al.* 2018; Domel *et al.* 2018; Guo *et al.* 2021; Du *et al.* 2022; Chen *et al.* 2023). The precise flow control mechanism, particularly how the effects of denticles differ from those of existing passive control structures, remains unknown.

Examining flow measurements around denticles poses challenges in physical experiments due to factors such as the diminutive size of the denticle features, typically in the order of 10 microns. Additionally, the complexity arises from the difficulties associated with laser arrangement and particle image velocimetry (PIV) measurements within the denticle array and beneath the crown. In this study, we examined the pore flow in two different scenarios using DNS so as to provide high-fidelity data at the denticle scale. One configuration is a zero pressure gradient (ZPG) flow, and the other is subjected to an adverse pressure gradient (APG) and flow separation. The objective is to justify

† Department of Mechanical Engineering, University of Mississippi

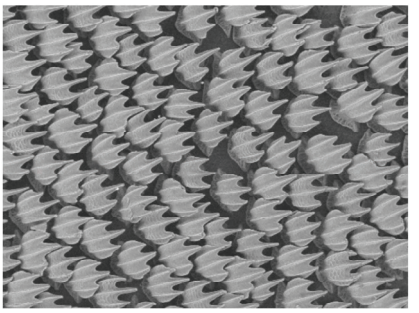

FIGURE 1. Bonnethead shark (*Sphyrna tiburo*) denticles from near the anal fin. Reproduced with permission from George Lauder of Harvard University (Lauder *et al.* 2016).

whether the cavity region below the denticle crown, an area not previously explored in the literature, has any hydrodynamic effects in various flow conditions. In the following, we first describe the configurations and numerical method. We then discuss the change of the pore flow due to pressure gradient and its role in drag reduction.

2. Simulation setup

DNS of turbulent channel flows over shark denticles were performed. Two configurations were employed to examine the pore flow under different flow and bristling conditions.

2.1. *Open channel configuration*

In this configuration, the bottom wall of an open channel is covered by shark denticle replicas, similar to the study by Boomsma & Sotiropoulos (2016). The denticles were either non-bristling (Case Chn0d) or bristling (Case Chn30d). Here, the bristling motion is defined as the rotation about the spanwise axis passing the centroid of the base. The angle of bristling is measured with respect to the base plane. The Reynolds number $Re_b = U_b H/\nu = 8{,}000$ in these two cases. Here, H is the channel half height, and U_b is the bulk velocity. A smooth-wall channel at this Reynolds number has a friction Reynolds number of approximately 450. The 3D model of a representative denticle from *Isurus oxyrinchus* (shortfin mako shark) provided by George Lauder of Harvard University is used. It was scanned using micro-CT and made symmetric about the spanwise direction (Wen *et al.* 2014) (shown in Figure 2). The height of the denticles for these two cases is $\delta_h = 0.0976H$, comparable to the one in Boomsma & Sotiropoulos (2016). What differentiates our study from previous studies is the inclusion of the neck of the denticle—a slender, cylinder-like structure situated underneath the wide lid-like crown (Figure 2(a)). In prior investigations, the neck has been omitted, with the research focus predominantly directed toward an analysis of streamwise ridges over the crown.

The denticles are offset by $\delta_x = 1.032\delta_w$ in the streamwise direction and $\delta_z = 1.142\delta_w$ in the spanwise (Figure 2(c)). Successive rows are staggered in the transverse plane by half of the spanwise spacing ($0.5\delta_z$). The spacings with respect to the denticle height chosen for this work mimic the arrangement of real shark denticles shown in Figure 1 and is the same arrangement that was 3D printed by Wen *et al.* (2014). A 56 by 24 array of denticles (1,134 total) covers the entire surface.

In Case Chn30d, the denticles are assigned a sinusoidal change of the bristling angle between 0 and 30 degrees of inclination. This range is chosen according to the average

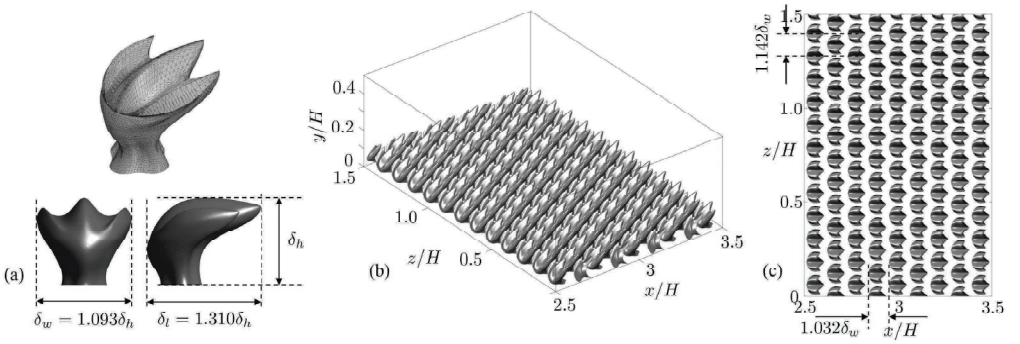

FIGURE 2. Schematic of (a) the denticle replica and (b,c) denticle array in Case Chn30d. Only part of the computational domain is shown. The denticle array is at the maximum bristling angle (see definition in text). The 3D CAD model of the denticle is provided by George Lauder of Harvard (Wen *et al.* 2014).

scale erection angle for the mid-flank region on the shortfin mako shark (Lang *et al.* 2011). When bristled at the maximum angle (30 degrees), the trailing edge of the denticle crown protrudes $0.0247H$ ($25\%\delta_h$) above the crown of non-bristled denticle (0 degrees), i.e., the effective wall-normal height of the denticle increases by 25% when at the maximum bristling angle. With the prescribed range of rotation, the denticles do not intersect one another. For the period of bristling, Du Clos *et al.* (2018) performed experiments with a piece of real flank skin and reported that the vortices in the near-wall wall turbulence create local APGs that bristle the denticle in a forward flow. Therefore, a time scale $T = 4.0H/U_b$, comparable to the bursting timescale of turbulence at this Reynolds number, is used here in Case Chn30d for the bristling period.

The computational domain is $6.16H \times 1.0H \times 2.92H$ in the streamwise (x), wall-normal (y), and spanwise (z) directions, respectively. The domain size in the x and z directions is close to the typical channel flow configurations and is adjusted to ensure the periodicity of the denticle array.

2.2. *Channel with bump configuration*

In this configuration, a parabolic bump is placed on the bottom wall of a turbulent full channel (Figure 3). This configuration has been utilized in our previous studies of flow separation (Wu 2021; Savino *et al.* 2023*a*); thus, the baseline dynamics are well understood. Note that the purpose of this configuration is not to make a direct comparison with the previous one, but to serve as a proof-of-concept study for denticle pore flow as a phenomenon that occurs in separation flows. Therefore, several changes aiming to achieve computational efficiency are applied. First, denticles are stationary in this study since no bristling mechanism during separation has been proven. Second, the simulation is performed at low Reynolds number $Re_b = 2,500$. Without the bump, this yields $Re_\tau \sim 165$. Third, only the lee side of the bump is covered by denticles. The APG over the lee side is more relevant to separating flows than the favorable pressure gradient (FPG) over the wind side, and a significant reduction in computation cost is achieved by covering only the lee side.

The bump is defined by $y/H = -0.15(x - 4.0)^2 + 0.25$. The height of the denticles is reduced to half of the one in the previous configuration (i.e., $\delta_h = 0.0488H$) such that the denticles are relatively small compared to the bump height. The lee side of the bump is indented by the new δ_h and covered by shark denticle replicas (refer to Figure

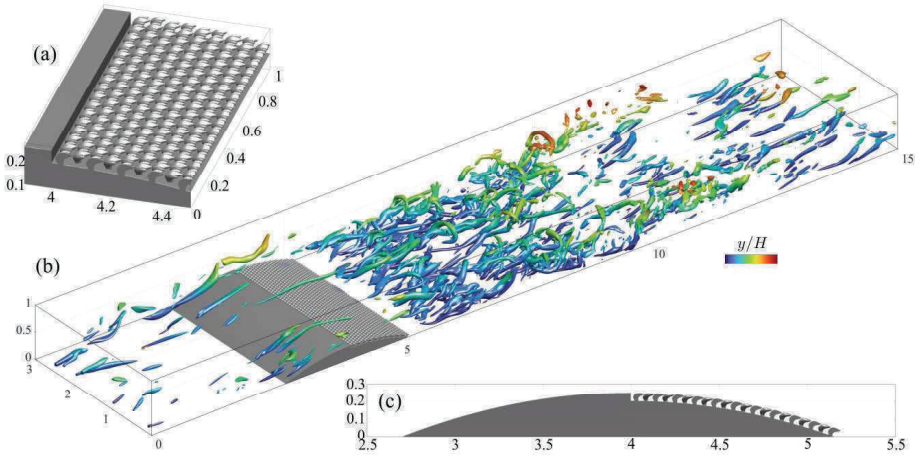

FIGURE 3. (a) 3-dimensional view of the lee-side denticle array. (b) Isometric view of computational domain with isosurfaces of the second invariant of the velocity gradient tensor shown to visualize the vortical structures in the separated shear layer. (c) Cut-plane visualizing cross section of the bump and denticle geometry. In all panels only part of the computational domain is shown for clarity.

3(c)). This ensures that the crests of the denticles align precisely with the contour of the smooth bump. The staggered denticle array is arranged with the same (50% smaller proportionally) spacing of $\delta_x = 1.032\delta_w$ and $\delta_z = 1.142\delta_w$. The orientation of each denticle row is adjusted so that the bump's local normal vector aligns with the vertical axis of the denticle. A 21 by 50 array of denticles (1,050 total) covers the entire lee side of the bump.

The computational domain for this case is $22.4H \times 2H \times 3.045H$ in the streamwise, wall-normal, and spanwise directions, respectively. Instantaneous velocity snapshots saved from an *a priori* channel flow at the same Reynolds number are used at the inflow. A convective boundary condition is used at the outflow. In the following discussion, we denote this case as Case BumpDent. Another simulation with the unmodified bump is also performed for comparison.

2.3. *Numerical methods*

The simulations are carried out using a well-established finite-difference solver that solves the incompressible Navier–Stokes equations on a Cartesian staggered grid (Keating *et al.* 2004; Wu & Piomelli 2018)

$$\frac{\partial u_i}{\partial x_i} = 0; \quad \frac{\partial u_i}{\partial t} + u_j \frac{\partial u_i}{\partial x_j} = -\frac{\partial p}{\partial x_i} + \frac{1}{Re}\frac{\partial^2 u_i}{\partial x_j^2} + f_i. \tag{2.1}$$

A second-order Adams–Bashforth scheme is employed for the convective terms, while the diffusion terms are discretized using an implicit Crank–Nicolson scheme. The spatial derivatives are computed using a second-order accurate central difference scheme. The Poisson equation is solved with a pseudo-spectral method using a combination of a complex Fourier transform in the spanwise direction followed by a direct inversion of a block tridiagonal matrix formed by the discretization of the two-dimensional Helmholtz equations. The complex geometries of the denticles are represented by an unstructured surface mesh with triangular elements. This surface grid is immersed in the fixed, non-body con-

formal Cartesian grid, and the boundary condition on the body surface is applied by an immersed boundary method based on the volume-of-fluid (VOF) approach through term f_i in Eq. (2.1) (Scotti 2006; Yuan 2015). For the bristling case, the VOF is updated every fifty timesteps ($0.0167H/U_b$, $\sim 0.42\%T$). The solver has shown great success in our previous studies of surface structures in turbulence including sandgrain roughness (Wu & Piomelli 2018; Wu *et al.* 2019), vortex generators (Savino *et al.* 2023*b*), and bumps (Wu 2021; Savino *et al.* 2023*a*).

Both the flow and the embedded structures are periodic in the spanwise direction. Spanwise two-point correlations show that fluctuating velocities are uncorrelated by half of the span near the wall and in the separated shear layer. In both configurations, the finest grid spacing is determined by the denticle features. For Cases Chn0d and Chn30d, the grid is uniform in the wall-parallel directions. In the wall-normal direction, it is uniform below the crest of the denticle and stretched toward the channel centerline. Each denticle is resolved by about 40^3 points. This resolution is comparable to the one used in Boomsma & Sotiropoulos (2016). The smallest radius of curvature is resolved by more than 3 points. In total, $1920 \times 400 \times 960$ (≈ 0.74 billion) grid points are used in the x, y, and z directions. In wall units, $\Delta x^+ = 2.3$, $\Delta y_1^+ = 0.8$, and $\Delta z^+ = 2.2$ for the high friction Reynolds number achieved in Case Chn30d. A finer grid (70^3 resolving each denticle), although not shown, results in negligible changes in flow statistics and less than 1% difference in drag. For the bump configuration, a grid with $N_x \times N_y \times N_z = 2016 \times 415 \times 2016$ (≈ 1.7 billion) grid points is used. The grid is uniform in the z direction; in the x and y directions, it is uniform for $x/H \in [4.0, 5.5]$ and $y/H < 0.25$ such that each denticle is resolved by 40 grid points in x, 50 in y, and 36 in z. Outside of the refined region, the grid is gradually stretched toward the inflow, outflow, and channel centerline. In wall units, $\Delta x^+ < 9.0$, $\Delta y_1^+ < 0.2$, and $\Delta z^+ < 0.25$. In regions distant from the wall, the maximum ratio between the Kolmogorov scale and the grid spacing is below 2 for $x/H \in [1.0, 9.0]$ and remains below 4 elsewhere.

The simulations are performed with a constant $\Delta t = 3.34 \times 10^{-4} H/U_b$ for the open channel configuration and $\Delta t = 2.1 \times 10^{-4} H/U_b$ for the bump. After a statistically steady state is reached, snapshots are collected every $0.5H/U_b$ over $200H/U_b$ to obtain statistics. The maximum Courant–Friedrichs–Lewy (CFL) number is approximately 0.5. The open channel simulations cost 1950 CPU hours per unit of time on 960 Xeon Platinum 8160 processors, and the bump simulations cost 2400 CPU hours per unit of time on 2016 processors. In the following discussion, quantities are averaged in time and in the spanwise direction over the fluid domain (i.e., intrinsic). The averaged quantities are denoted as capital letters for primary flow variables and by $\overline{(.)}$ for turbulent statistics. For Case Chn30d, phase averaging is performed to conditionally sample the flow field at eight equally spaced phases of a bristling period to examine the temporal evolution of pore flow. Operator $\langle . \rangle$ is used to denote the phase-averaged quantities.

3. Results and discussion

3.1. *Open channel configuration*

We observed that the pore flow is negligible in Cases Chn0d and Chn30d. Figure 4(a) shows the mean and phase-averaged velocity in the two cases. For the non-bristling case, the mean flow is everywhere positive. The pore flow under the crown of the denticle has a peak magnitude of $0.0072U_b$ at $20\%\delta_h$. When the denticles are bristling, the mean pore flow deep in the cavity region does not change. At $0.67\delta_h$, on the contrary, the

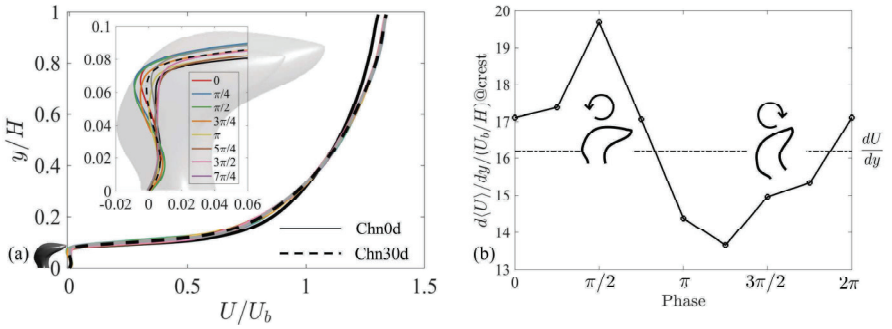

FIGURE 4. Plots of (a) mean and phase-averaged velocity and (b) phase-averaged shear at the crest of the denticle during a bristling cycle. The side view of the denticle is superposed in panel (a) for reference.

mean velocity is reduced to close to zero. The bristling introduces a periodic temporal variation of the phase-averaged velocity. There is a backward flow around the crown when the denticles are bristling up and a forward one when the denticles return to the flat position. A slightly elevated forward pore flow is observed during the bristling-up stage of a cycle. Note that the phase-average velocity profiles are not symmetric between the bristling-up and -down stages. If we consider the flow over the crown of the denticles, it is subjected to a varying velocity gradient during a bristling cycle. Figure 4(b) is the phase-averaged shear measured at the height of a non-bristled denticle. It can be seen that it peaks before reaching the maximum bristling angle and decreases to the lowest value before the denticle returns to the flat position. Between different phases, the mean shear experienced by the passing fluid can vary by more than 45%.

The flow around the denticle exhibits rich spatial variations (see Figure 5). Without bristling, the flow tends to be deflected into the cavity region when it impinges on the rounded front of the crown. As it travels downward, the pore fluid moves around the necks of the denticles, forming a weak acceleration (refer to the slices at $50\%\delta_h$ in Figure 5(a)). After passing the necks, the flow escapes back toward the ambient flow through the gaps between the three ridges. When the assigned bristling is enabled, the inclined denticle protrudes into the flow and deflects more fluid to enter the cavity region. This is most significant at the maximum bristling angle and when the denticle begins to recover to the flat position (Figure 5(g-j)). However, this injection into the cavity region does not form a net mean flow: as the denticles bristle up (before they reach the maximum angle), the region shielded by the crown is reduced, allowing the previously injected pore flow to escape back to the outer region (Figure 5(f)).

Similar to the study of Boomsma & Sotiropoulos (2016), our results show a significant increase in drag compared to a smooth channel. The friction Reynolds number increases from 450 to 664 for Case Chn0d and 722 for Case Chn30d. The mean streamwise force exerted by the fluid on the denticle, i.e., $-\overline{f}_x$ term in Eq. (2.1), is plotted in Figure 6(a). It can be observed that the bristling changes mainly the drag force ($-\overline{f}_x > 0$) in the crown region, while the region below $0.06H$ (or 62% of the denticle height) does not produce a significant force. The spanwise spacing between the denticle ridges is $s = 0.417\delta_w$. At these Reynolds numbers, it gives $s^+ = 25$ and 27, respectively. Both are above the optimal drag-reduction spacing for riblets (García-Mayoral & Jiménez 2011). The effective roughness height, k_s, can be obtained by measuring the downshift of the velocity profile in wall units in the log-law region. It gives $k_s^+ = 33$ and 64 for the two

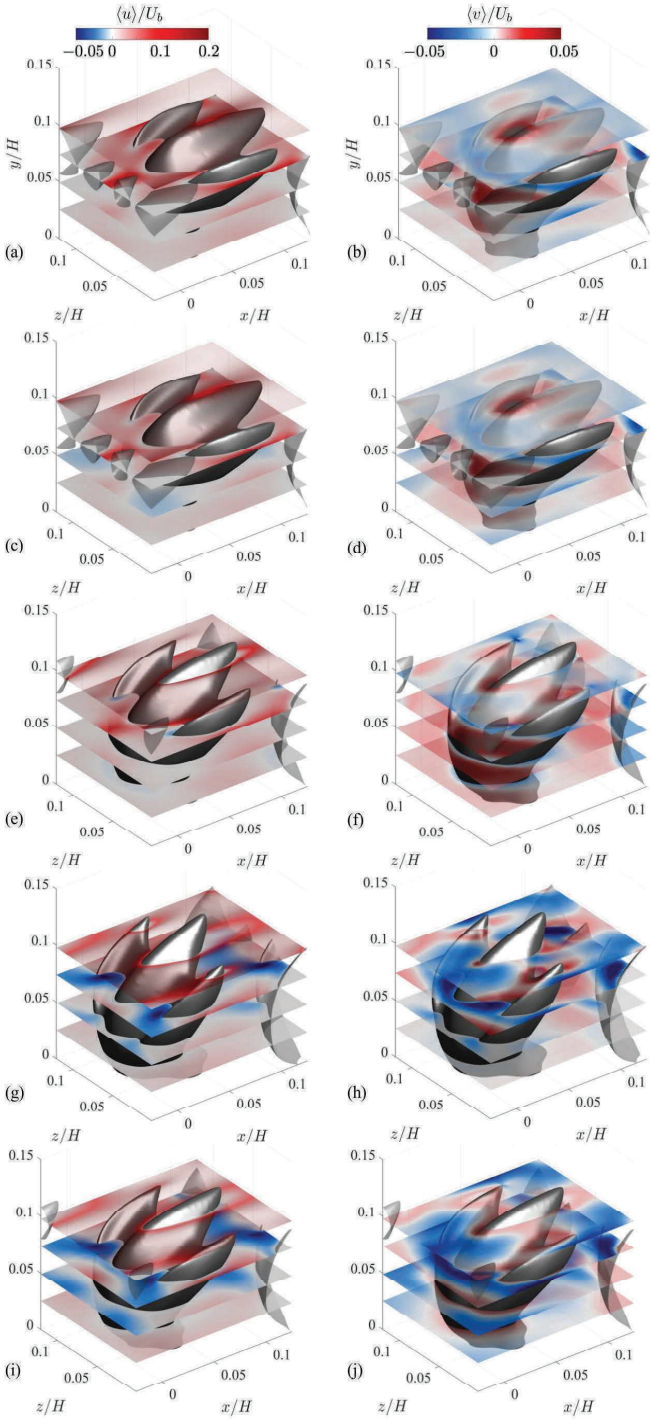

FIGURE 5. Temporal- and ensemble-averaged velocity around the denticle. (a,b) Case Chn0d, (c-j) Case Chn30d. Left column, streamwise component; right column, wall-normal component. (c,d) phase 0, (e,f) phase $\pi/2$, (g,h) phase π, (i,j) phase $3\pi/2$. The visualizations are made at 25%, 50%, 75%, and 100% denticle height.

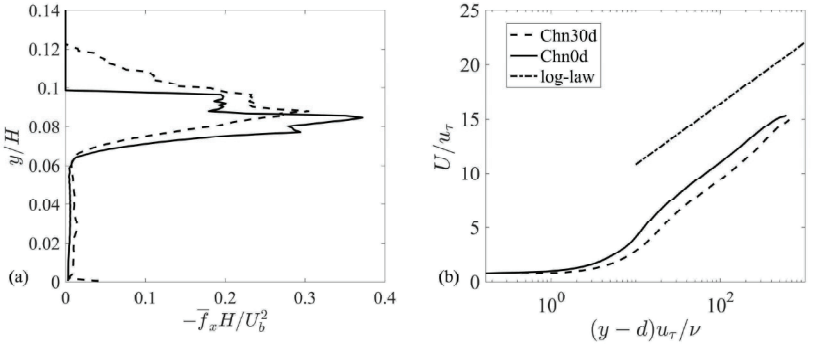

FIGURE 6. Profiles of (a) mean streamwise force exerted by the fluid on the denticle and (b) mean velocity in wall units, where d is the zero-plane displacement calculated as the centroid of $\overline{f_x}$.

cases. Our results show a significant drag increase compared to Boomsma & Sotiropoulos (2016). This may be due to the higher Reynolds number (3X in our case), as drag has been proven to be predominantly produced by viscous friction (Boomsma & Sotiropoulos 2016). Indeed, in their study, the denticle crown produces a $k_s^+ = 6.2$, indicating a nearly hydraulically smooth surface. The denticles in our cases are transitionally rough in Case Chn0d and fully rough in Chn30d.

In summary, our study of denticles in ZPG channel flow indicates that the pore flow in the cavity region has little effect on the flow over the denticles and the drag. However, as we show in the next section, it plays an important role when the flow is subjected to APGs followed by a turbulent separation. In addition, our results agree with the previous studies of realistic shark denticle structures that they do not reduce drag. Despite that the ridges over the crown resemble streamwise riblets, the complex geometry of the denticle creates local high shear and recirculation, leading to a significant drag increase.

3.2. *Channel with bump configuration*

Figure 7 shows the instantaneous streamwise velocity over the bump and on the bottom wall of the channel in Case BumpDent. Local reversed flow due to the APG can be observed over the denticle replicas. The mean flow detaches from the crest of the denticles at $x/H = 4.56$ and reattaches on the flat wall downstream at $x/H = 6.25$, yet significant spatial variation of instantaneous reversed flow can be observed. Figure 8(a) is the contour of the mean streamwise velocity. The outlines of the denticles are superposed for reference. Note that streamwise successive rows are staggered in the span. Unlike in the ZPG open channel configuration, the pore flow in this configuration exhibits a distinct feature. A reversed flow beneath the denticle crown prior to the onset of massive flow separation can be seen. This pore flow has a relatively small magnitude reaching approximately $0.025U_b$, about half of the friction velocity. Locally, it shows a peak that is at $\sim$30% of the denticle height from the base, occurring in the middle of the neck. Interestingly, the reversed pore flow diminishes once the massive separation occurs.

The reversed pore flow increases the thrust, i.e., the reversed friction and back pressure on the lee side of the bump that is in the positive x direction, by threefold compared with the smooth bump. This indicates a drag-reduction mechanism that the sharks may utilize. The distribution of the average $-f_x$ term in Eq. (2.1) is visualized in Figure 8(b). It is the total force including both the pressure force and the viscous force. $-\overline{f}_x > 0$

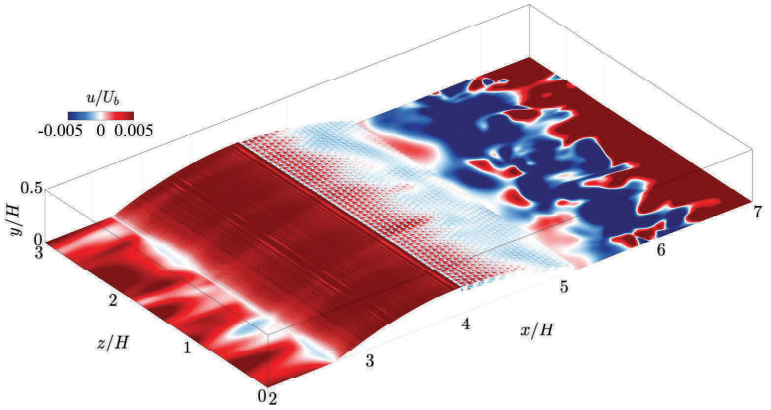

FIGURE 7. Instantaneous streamwise velocity over the bottom wall of the channel and the bump in Case BumpDent. The color bar is saturated to better show the reversed flow over the denticle crowns.

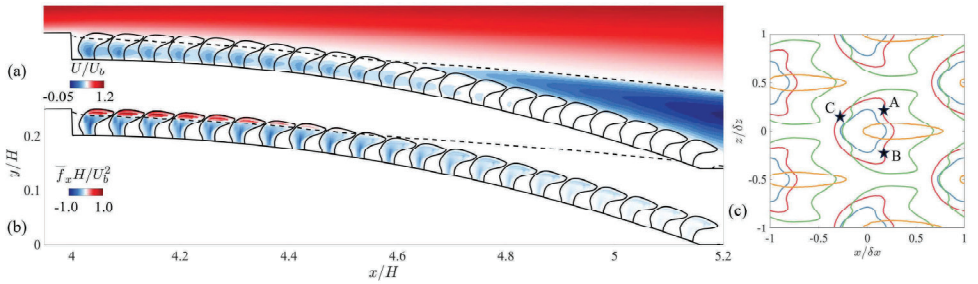

FIGURE 8. (a) Mean streamwise velocity distribution over the denticle bump. (b) Mean streamwise force exerted by the denticles on the fluid (negative of f_x in Eq. (2.1)). Positive values represent drag, and negative ones indicate thrust. In panels (a) and (b), the dashed line represents $U = 0$. (c) Outlines of a denticle and its neighbors at selected heights from the denticle base: —— base, —— $25\%\delta_h$, —— $50\%\delta_h$, and —— $75\%\delta_h$.

indicates the solid is impeding the fluid's forward motion, thereby leading to a drag. Conversely, a negative contour indicates a thrust. The surface of the indented bump that is not covered by the denticle base also contributes to the total force (not shown). It can be seen that the majority of the denticles are producing thrust. The most significant thrust contribution coincides with the prominent reversed pore flow around the denticle neck. Specifically, the peak thrust corresponds to the backward-facing bulges on the side of the neck (Points A and B at $25\%\delta_h$ in Figure 8(c)). The thrust distribution indicates that it is generated by the friction when the pore flow moves around the denticle neck, as well as the pressure when it impinges on the backward-facing side bulges. Additionally, the blunt front of the denticle neck (surface passing Point C at $25\%\delta_h$ in Figure 8(c)), which acts as a mildly diverging surface for the reversed pore flow, appears to be optimized to prevent local separation, as no drag is observed over the neck's leading edge.

We call this mechanism of reversed pore flow passing denticle necks a channeling effect. To examine its 3D features, we performed a temporal average followed by an ensemble average between the 50 denticles along the span (denoted by operator $\langle\bar{\cdot}\rangle$). Figure 9 shows the velocity vector around denticles at select streamwise locations, colored by $\langle\bar{u}\rangle$. The reverse pore flow goes around the neck of the denticle and is accelerated, forming a jet that

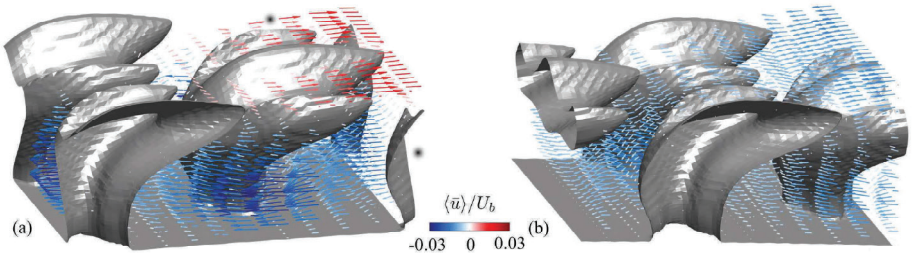

FIGURE 9. Temporal- and ensemble-averaged velocity vector field around denticles: (a) $x/H = 4.3$ and (b) $x/H = 4.6$. The arrows are colored by the streamwise component. The mean separation point is at $x/H = 4.56$.

strikes the back of the neck of upstream denticles. The spanwise staggered arrangement of the denticle array utilizes the channeling effect to produce thrust. Note that Evans *et al.* (2018), in their separation over a cylinder array experiment, hypothesized that a pore flow in the same direction as the boundary layer over the array is responsible for the momentum transfer between the boundary layer and the pore flow. Our results indicate this is not the case. The most significant thrust-generating pore flow is in the opposite direction as the flow over the crown, i.e., upstream.

4. Conclusions

Pore flow underneath the crown of shark denticles is investigated using two configurations: ZPG open channel and separating flow over the lee side of a bump. DNS are performed with the embedded denticles represented by an immersed boundary method. For ZPG channel flow, the pore flow is negligible regardless of whether the denticles are stationary or bristling. Agreeing with previous studies in which the complex geometry of the denticles is considered, our results show a drag increase. When the stationary denticles are applied to the lee side of a bump, a reversed pore flow is formed in the cavity region underneath the crown. It significantly increases the thrust on the lee surface, indicating a thrust-generating mechanism. Further investigation of this mechanism is ongoing. The simulations in the current study are constrained to specific values for various parameters, such as the bristling angle, period, ratio between denticle height and channel half height, Reynolds number, and bump configuration, which are different from realistic shark skin and flow conditions. Further parametric studies are warranted.

Acknowledgments

This investigation was funded by NSF Grant #OIA-2131942. B.S. appreciates the support of the NSF GRFP Award #2235036. The simulations were performed on TACC Stampede-2 clusters sponsored by NSF. The authors thank Drs. Parviz Moin, Beverley McKeon, Ugo Piomelli, Thomas Jaroslawski, and Mr. Rahul Agrawal for fruitful discussion.

REFERENCES

BECHERT, D., HOPPE, G. & REIF, W. E. 1985 On the drag reduction of the shark skin. In *23rd Aerosp. Sci. Meeting*, pp. 1–18.

Boomsma, A. & Sotiropoulos, F. 2016 Direct numerical simulation of sharkskin denticles in turbulent channel flow. *Phys. Fluids* **28**, 035106.

Chen, G.-Q., Du, Z.-Z., Li, H.-Y., Lv, P.-Y. & Duan, H.-L. 2023 On the drag reduction of an inclined wing via microstructures with the immersed boundary-lattice Boltzmann flux solver. *Phys. Fluids* **35**, 087105.

Devey, S. P., Lang, A. W., Hubner, J. P., Morris, J. A. & Habegger, M. L. 2018 Experimental analysis of passive bristling in air to enable mako-shark-inspired separation control. *AIAA Paper* 2768.

Domel, A. G., Saadat, M., Weaver, J. C., Haj-Hariri, H., Bertoldi, K. & Lauder, G. V. 2018 Shark skin-inspired designs that improve aerodynamic performance. *J. R. Soc. Interface* **15**, 20170828.

Doosttalab, A., Dharmarathne, S., Evans, H. B., Hamed, A. M., Gorumlu, S., Aksak, B., Chamorro, L. P., Tutkun, M. & Castillo, L. 2018 Flow modulation by a mushroom-like coating around the separation region of a wind-turbine airfoil section. *J. Renew. Sustain. Ener.* **10**, 043305.

Du, Z., Li, H., Cao, Y., Wan, X., Xiang, Y., Lv, P. & Duan, H. 2022 Control of flow separation using biomimetic shark scales with fixed tilt angles. *Exp. Fluids* **63**, 1–12.

Du Clos, K. T., Lang, A., Devey, S., Motta, P. J., Habegger, M. L. & Gemmell, B. J. 2018 Passive bristling of mako shark scales in reversing flows. *J. R. Soc. Interface* **15**, 20180473.

Evans, H. B., Hamed, A. M., Gorumlu, S., Doosttalab, A., Aksak, B., Chamorro, L. P. & Castillo, L. 2018 Engineered bio-inspired coating for passive flow control. *P. Natl. Acad. Sci. U.S.A.* **115**, 1210–1214.

García-Mayoral, R. & Jiménez, J. 2011 Drag reduction by riblets. *Philos. T. Roy. Soc. A* **369**, 1412–1427.

Guo, P., Zhang, K., Yasuda, Y., Yang, W., Galipon, J. & Rival, D. E. 2021 On the influence of biomimetic shark skin in dynamic flow separation. *Bioinspir. Biomim.* **16**, 034001.

Keating, A., Piomelli, U., Bremhorst, K. & Nešić, S. 2004 Large-eddy simulation of heat transfer downstream of a backward-facing step. *J. Turbul.* **5**, N20

Lang, A., Motta, P., Habegger, M. L., Hueter, R. & Afroz, F. 2011 Shark skin separation control mechanisms. *Mar. Technol. Soc. J.* **45**, 208–215.

Lang, A. W., Motta, P., Hidalgo, P. & Westcott, M. 2008 Bristled shark skin: a microgeometry for boundary layer control? *Bioinspir. Biomim.* **3**, 046005.

Lauder, G. V., Wainwright, D. K., Domel, A. G., Weaver, J. C., Wen, L. & Bertoldi, K. 2016 Structure, biomimetics, and fluid dynamics of fish skin surfaces. *Phys. Rev. Fluids* **1**, 060502.

Lloyd, C. J., Mittal, K., Dutta, S., Dorrell, R. M., Peakall, J., Keevil,a G. M. & Burns, A. D. 2023 Multi-fidelity modeling of shark skin denticle flows: insights into drag generation mechanisms. *R. Soc. Open Sci.* **10**, 220684.

Oeffner, J. & Lauder, G. V. 2012 The hydrodynamic function of shark skin and two biomimetic applications. *J. Exp. Biol.* **215**, 785–795.

Santos, L. M., Lang, A., Wahidi, R., Bonacci, A., Gautam, S., Devey, S. & Parsons, J. 2021 Passive separation control of shortfin mako shark skin in a turbulent boundary layer. *Exp. Therm. Fluid Sci.* **128**, 110433.

Savino, B., Patel, D. & Wu, W. 2023*a* Reynolds-number dependence of separating

flow over a bump in spanwise rotating channel flows. In *Direct and Large-Eddy Simulation XIII*, 41–46.

Savino, B., Yeom, T. & Wu, W. 2023*b* Numerical study of turbulent characteristics behind novel vortex generating structures. *AIAA Paper* 0091.

Scotti, A. 2006 Direct numerical simulation of turbulent channel flows with boundary roughened with virtual sandpaper. *Phys. Fluids* **18**, 031701.

Wen, L., Weaver, J. C. & Lauder, G. V. 2014 Biomimetic shark skin: design, fabrication and hydrodynamic function. *J. Exp. Biol.* **217**, 1656–1666.

Wu, W. 2021 Flow separation behind a bulge in rotating turbulent channel flows. In *APS Div. Fluid Dyn. Meeting*, Abstract id.E16.002.

Wu, W. & Piomelli, U. 2018 Effects of surface roughness on a separating turbulent boundary layer. *J. Fluid Mech.* **841**, 552–580.

Wu, W., Piomelli, U. & Yuan, J. 2019 Turbulence statistics in rotating channel flows with rough walls. *Int. J. Heat Fluid Fl.* **80**, 108467.

Yuan, J. 2015 Numerical simulations of rough-wall turbulent boundary layers. PhD thesis, Queen's University.